Shape optimisation of the building facade energy efficiency in transient regime

Sultan Alpar, Julien Berger, Rafik Belarbi

Shape optimisation of the building facade energy efficiency in transient regime

Sultan ALPAR [1,*], Julien BERGER [1], Rafik BELARBI [1]

July 22, 2024

[1] Laboratoire des Sciences de l'Ingénieur pour l'Environnement (LaSIE), UMR 7356 CNRS, La Rochelle Université, CNRS, 17000, La Rochelle, France
*corresponding author, e-mail address : sultan.alpar@univ-lr.fr

Abstract

The current research lacks sufficient studies on optimizing shapes for managing transient heat transfer in building enclosures. This gap is primarily due to numerical challenges in optimizing shapes for this purpose. This article aims to address and bridge these gaps by investigating the energy efficiency of a building wall through the optimization of its external boundary shape. The study assumes two-dimensional transient heat diffusion to represent the physical phenomena in the building facade, considering a third type boundary condition for the outside boundary, including convective and short-wave solar radiation effects. The internal boundary condition is modeled using the Robin boundary condition. The boundary element method is employed to solve the transient heat transfer problem, reducing computational costs while ensuring accuracy. The optimization problem focuses on minimizing the heat losses of the wall by finding optimal parameters for the external boundary. A real case study on a house wall reveals optimal shapes, maintaining the same material quantity as standard flat wall and increasing energy efficiency.

Keywords: transient heat transfer, boundary element method, shape optimization, short wave radiation.

1 INTRODUCTION

One third of the global energy consumption and one fifth of greenhouse gas emissions is contributed by buildings, according to the 2022 statistics from the International Energy Agency (IEA) in Paris, France [1]. Over the past half century, efforts to enhance the energy efficiency of building enclosures have led to various models and simulation programs [2]. However, these designs often rely on two principles: a) treating enclosures as plane barriers against varying climatic conditions, disregarding non-uniform distribution of incident radiation and convective heat flux [3]; and b) utilizing a 1D model through the combination of multiple plane layers [4].

The primary focus of this article is to explore the potential improvement of energy efficiency through the shape optimization of building facades. Notable research in building facade shape optimization includes studies on minimizing wind-induced loads in high-rise buildings [5] and multi-objective optimization for sustainable high-rise buildings [6].

The first challenge in shape optimization lies in parametrizing the shape, with continuous and discrete approaches being prominent [7]. Continuous parameterization involves mathematical equations for smooth transitions between shapes, but it demands significant computational resources. Conversely, discrete parameterization uses a finite set of parameters, making it suitable for representing more complex real-world shapes. However, it explores only a limited part of the parameter domain, potentially missing optimal shapes.

The second challenge involves modeling physical phenomena in building enclosures. Existing works often neglect or simplify heat transfer through solid walls, emphasizing fluid flow dynamics around enclosures [8]. This oversight misses the crucial energy balance played by solid facades between the inside and outside environment [9]. Additionally, there is limited attention given to the impact of solar radiation on building shape and design [10]. Another drawback of existing works is considering steady-state models for building surface shape design [11].

To address these challenges, this research investigates transient heat transfer mechanisms through building walls, considering the impact of incident short-wave radiation and incorporating a continuous description of the building wall shape. The boundary element method (BEM) is employed for computational efficiency without compromising accuracy. The article is organized as follows: Section 2 presents governing equations with appropriate boundary conditions. It continues with the description of the numerical method for the direct problem. Section 3 outlines the design optimization problem, while Section 4 verifies BEM with analytical solutions. Finally, Section 5 presents a real case study for the facade shape optimization during winter and summer periods.

2 METHODOLOGY

2.1 Physical domain

The physical domain under investigations is illustrated in Figure 1. The domain is denoted by Ω with space coordinates $\boldsymbol{x} = (x, y)$. The height of the facade is H [m]. The boundary of the domain is $\Gamma = \cup_{i=1}^{4} \Gamma_i$. The bottom, right and top boundaries are denoted as Γ_2, Γ_3 and Γ_4, respectively. The left boundary is Γ_1 and is defined by:

$$\Gamma_1(\boldsymbol{p}) = \{\boldsymbol{x} \in \mathbb{R}^2 \,|\, x = \gamma(\boldsymbol{p}, y), y \in [0, H], \boldsymbol{p} \in \Omega_p\}, \tag{1}$$

where $\gamma(\boldsymbol{p}, y)$ is a parametrized mapping function, which shapes the form of the boundary Γ_1 depending on the N_p parameters:

$$\boldsymbol{p} = (p_1, \ldots, p_{N_p}) \in \Omega_p.$$

Note that in the case $\gamma(\boldsymbol{p}, y) = 0$, we have a plane boundary Γ_1 and the facade is a classical rectangular one. In such case, the length of the wall is denoted L [m].

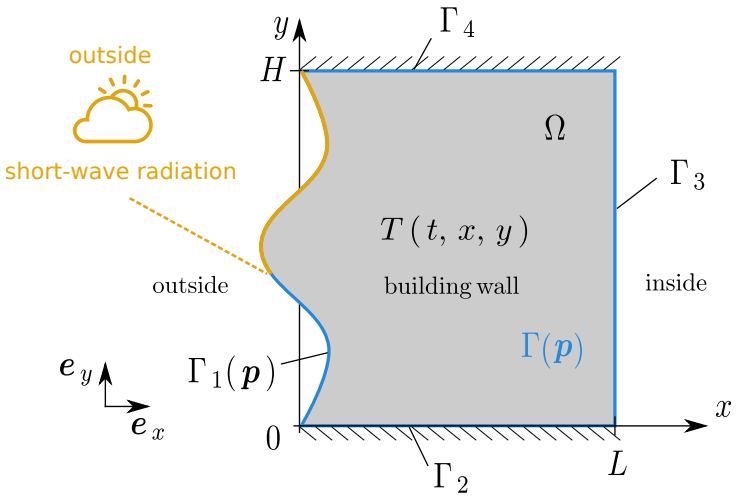

Figure 1. *Illustration of the physical domain.*

2.2 Governing equations

The physical process are observed for the time domain $\Omega_t : t \in [0, t_\infty]$, where t_∞ [s] is the total duration time. The two-dimensional transient heat diffusion transfer is assumed to represent the physical phenomena in the building facade:

$$c\,\rho\,\frac{\partial T}{\partial t} \;=\; k\,\boldsymbol{\Delta}\,T\,, \qquad \forall\, t \,\in\, \Omega_t\,, \qquad \forall\, \boldsymbol{x} \,\in\, \Omega\,, \tag{2}$$

where c [$\mathrm{J \cdot kg^{-1} \cdot K^{-1}}$] is the specific heat capacity, ρ [$\mathrm{kg \cdot m^{-3}}$] is the material density, k [$\mathrm{W\,.\,m^{-1}\,.\,K^{-1}}$] is the thermal conductivity of the wall and T [K] is the temperature inside the facade. The initial conditions of the problem is given as:

$$T\,(\boldsymbol{x},\, t=0) \;=\; T_0\,(\boldsymbol{x})\;, \qquad \forall\, t \,\in\, \Omega_t\,, \qquad \forall\, \boldsymbol{x} \,\in\, \Omega\,. \tag{3}$$

The left boundary is in contact with the outside environment of the building. Combining Newton's law of heat transfer with Fourier's first law of conduction and adding the incident short-wave solar radiation leads us to a third-type boundary condition also known as Robin boundary condition:

$$k\,\boldsymbol{\nabla}\,T \cdot \vec{\boldsymbol{n}} \;=\; -\,h_L^\infty\,(t,\,y)\,(T \;-\; T_L^\infty) \;+\; q_L^\infty\,(t,\,\boldsymbol{x})\,, \qquad \forall\, t \,\in\, \Omega_t\,, \qquad \forall\, \boldsymbol{x} \,\in\, \Gamma_1\,,$$

where h_L^∞ [$\mathrm{W\,.\,m^{-2}\,.\,K^{-1}}$] is the surface heat transfer coefficient between the solid material and the surrounding fluid (air) with the temperature T_L^∞ [K]. The incident flux q_L^∞ [$\mathrm{W\,.\,m^{-2}}$] varies with the height of the facade due to the surrounding effects of the urban area and due to the shape of the boundary that may induce local shadings [12]. The surface heat transfer coefficient h_L^∞ depends on height y [m] and the according wind velocity v_∞ [$\mathrm{m\,.\,s^{-1}}$] [13]:

$$h_L^\infty\,(t,\,y) \;=\; h_0 \;+\; h_1\,\frac{v_\infty(t)}{v_0}\left(\frac{y}{y_0}\right)^{\lambda},$$

where h_0, h_1 [$\mathrm{W\,.\,m^{-2}\,.\,K^{-1}}$] and λ [$-$] are given surface coefficients and the velocity variation coefficient respectively. v_0 [$\mathrm{m\,.\,s^{-1}}$] and y_0 [m] are reference quantities.

The incident short-wave radiation on a tilted surface can be decomposed as follows [14]:

$$q_L^\infty\,(\boldsymbol{x}) \;=\; a\,(\,q^{\,\mathrm{dr}}\,(\boldsymbol{x}) \;+\; q^{\,\mathrm{df}}\,(\boldsymbol{x}) \;+\; q^{\,\mathrm{rf}}\,(\boldsymbol{x})\,), \tag{4}$$

where direct $q^{\,\mathrm{dr}}$ [$\mathrm{W\,.\,m^{-2}}$], diffusive $q^{\,\mathrm{df}}$ [$\mathrm{W\,.\,m^{-2}}$] and reflective $q^{\,\mathrm{rf}}$ [$\mathrm{W\,.\,m^{-2}}$] fluxes are components of the incident short-wave radiation. a is the absorptivity of the wall.

The right boundary is in contact with the ambient air inside of the building so a Robin boundary condition is assumed:

$$k\,\boldsymbol{\nabla}\,T \cdot \vec{\boldsymbol{n}} \;=\; -\,h_R^\infty\,(T \;-\; T_R^\infty\,(t))\,, \qquad \forall\, t \,\in\, \Omega_t\,, \qquad \forall\, \boldsymbol{x} \,\in\, \Gamma_3\,,$$

where T_R^∞ [K] is the known inside ambient temperature and h_R^∞ [$\mathrm{W\,.\,m^{-2}\,.\,K^{-1}}$] is the surface heat transfer coefficient inside the building. Last, the top and bottom boundaries of the facade are assumed as adiabatic:

$$k\,\boldsymbol{\nabla}\,T \cdot \vec{\boldsymbol{n}} \;=\; 0\,, \qquad \forall\, t \,\in\, \Omega_t\,, \qquad \forall\, \boldsymbol{x} \,\in\, \Gamma_2 \,\cup\, \Gamma_4\,.$$

Note that for computational purposed [15], a dimensionless formulation of the equations is defined [16] and all methodology is described for dimensionless variables.

2.3 Numerical method to solve the direct problem

2.3.1 Dual reciprocity method

In the view of the dual reciprocity boundary element method [17], the transient heat Eq. (2) is rewritten as:

$$\boldsymbol{\Delta}\, u \;=\; b\,(\,\boldsymbol{x}\,,\,u\,), \tag{5}$$

where:

$$b\,(\,\boldsymbol{x}\,,\,u\,) \;=\; \frac{\partial u}{\partial t}\,. \tag{6}$$

The solution to Eq. (5) can be expressed as the sum $u = \Phi + \hat{u}$, where Φ is the solution of homogeneous Laplace's equation and $\hat{u}$ is the particular solution, such that:

$$\boldsymbol{\Delta}\,\hat{u} \;=\; b\,. \tag{7}$$

It is generally difficult to find a solution that satisfies the above, particularly in the case of non-linear time-dependent problems. The dual reciprocity method proposes the use of a series of particular solutions $\hat{u}_k$ instead of a single function $\hat{u}$. If there are N_e boundary nodes and N_i internal nodes, there will be $(\,N_e \;+\; N_i\,)$ values of $\hat{u}_k$. The following approximation for b is proposed:

$$b\,(\,\boldsymbol{x}\,,\,u\,) \approx \sum_{k=1}^{N_e\,+\,N_i} \mu_k\, f_k\,(\,\boldsymbol{x}\,)\,, \tag{8}$$

where the μ_k are a set of initially unknown coefficients and the f_k are approximating functions, which can be compared to the usual interpolation functions [18]. In order to define these functions it is customary to propose an expansion for f:

$$f\,(\,\boldsymbol{x}\,) \;=\; 1 \;+\; r\,(\,\boldsymbol{x}\,)\,. \tag{9}$$

where r is the distance from a source point to a boundary point, which is defined as:

$$r(\,\boldsymbol{x}\,) \;=\; \Big[\;(\,x \;-\; x_\xi)^2 \;+\; (\,y \;-\; y_\xi)^2\;\Big]^{1/2}.$$

Here $\boldsymbol{x}_\xi \;=\; (\,x_\xi\,,\,y_\xi\,)$ is a source point coordinates and $\boldsymbol{x} \;=\; (x,\,y)$ is a boundary point coordinates, which is shown in Fig. 2(a).

The series of particular solutions $\hat{u}_k$ and the approximating functions f_k are related through the relation:

$$\boldsymbol{\Delta}\,\hat{u}_k \;=\; f_k\,. \tag{10}$$

Thus, in this case $\hat{u}$ and $\hat{q}$ can be found as:

$$\begin{aligned} \hat{u}\,(\,\boldsymbol{x}\,) \;&=\; \frac{r^2\,(\,\boldsymbol{x}\,)}{4} \;+\; \frac{r^3\,(\,\boldsymbol{x}\,)}{9}\,, \\ \hat{q}\,(\,\boldsymbol{x}\,) \;&=\; \Big(\frac{\partial r}{\partial x}\,\frac{\partial x}{\partial n} \;+\; \frac{\partial r}{\partial y}\,\frac{\partial y}{\partial n}\Big)\Big(\frac{1}{2} \;+\; \frac{r\,(\,\boldsymbol{x}\,)}{3}\Big)\,. \end{aligned} \tag{11}$$

Substituting Eq. (10) into Eq. (8) gives:

$$b \approx \sum_{k=1}^{N_e\,+\,N_i} \mu_k\,(\boldsymbol{\Delta}\hat{u}_k)\;. \tag{12}$$

Eq. (12) can be substituted into the original equation Eq. (**??**) to give the following expression:

$$\boldsymbol{\Delta} u \;=\; \sum_{k=1}^{N_e \,+\, N_i} \mu_k \, (\boldsymbol{\Delta} \hat{u}_k) \; . \tag{13}$$

Eq. (13) can be multiplied by Φ, which is the fundamental solution of LAPLACE's equation and integrated over domain, producing:

$$\int_\Omega (\boldsymbol{\Delta}\, u \,) \, \Phi \, d\Omega \;=\; \sum_{k \,=\, 1}^{N_e \,+\, N_i} \mu_j \int_\Omega (\boldsymbol{\Delta}\, \hat{u}_j \,) \, \Phi \, d\Omega \,, \tag{14}$$

where Φ is defined by :

$$\Phi \;=\; -\, \frac{\ln (r \,)}{2\, \pi},$$

2.3.2 Boundary integral equation

To obtain a Boundary Integral Equation (BIE) relating to boundary values, integral by parts is taken from the Laplacian terms in Eq. (14) and the limit is taken when the point $\boldsymbol{x}_\xi$ tends to a point $\boldsymbol{x}$ on the boundary Γ. However, if $\boldsymbol{x}_\xi$ belongs to the boundary Γ, the limits produce what is called a free term. Taking into account these terms produces the following BIE for each source node $\boldsymbol{x}_\xi$:

$$c_\xi \, u_\xi \;+\; \int_\Gamma q^* u \, d\Gamma \;-\; \int_\Gamma \Phi \, q \, d\Gamma \;=\; \sum_{k=1}^{N_e \,+\, N_i} \mu_k \left(c_\xi \, \hat{u}_{\xi\, k} \;+\; \int_\Gamma q^* \, \hat{u}_k \, d\Gamma \;-\; \int_\Gamma \Phi \, \hat{q}_k \, d\Gamma \right) \,, \tag{15}$$

where q and q^* are normal derivatives for u and Φ:

$$q \;=\; \nabla u \cdot \vec{\boldsymbol{n}} \,, \quad q^* \;=\; \nabla \Phi \cdot \vec{\boldsymbol{n}} \,,$$

The free coefficient c_ξ in Eq. (15) is given by:

$$c_\xi \;=\; \frac{\alpha}{2\, \pi} \,, \qquad 0 \,\leq\, c_\xi \,\leq\, 1,$$

where α is an internal angle at source point $\boldsymbol{x}_\xi$.

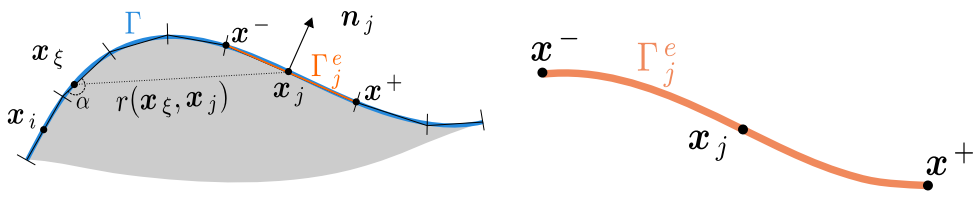

(a) (b)

Figure 2. *Illustration of the approximation of the whole boundary* Γ (a) *and of one boundary element* Γ_j (b).

2.3.3 Discrete Boundary Integral equation

The BIE (15) can only be solved analytically for some very simple problems. For this, a standard GREEN's function method is normally used. Rather than attempting analytical solutions to the BIE for particular geometries and boundary conditions, we seek a suitable reduction of the equation to an algebraic form that can be solved by a numerical approach.

The Boundary Element Method (BEM) is a numerical method of solution of the BIE, based on a discretization procedure [19]. Application requires two types of approximation: the first geometrical, involving a subdivision of the boundary Γ into N_e small segments or elements Γ_j, schematically shown in Fig. 2(b), such that:

$$\Gamma \approx \sum_{j=1}^{N_e} \Gamma_j \, .$$

Taking this into account, Eq. (15) can be written in the form:

$$c_i \, u_i \; + \; \sum_{j=1}^{N_e} \int_{\Gamma_j} q^* \, u \, d\Gamma \; - \; \sum_{j=1}^{N_e} \int_{\Gamma_j} \Phi \, q \, d\Gamma \; = \; \sum_{k=1}^{N_e \, + \, N_i} \mu_k \left(c_i \, \hat{u}_{ik} \; + \; \sum_{j=1}^{N_e} \int_{\Gamma_j} q^* \, \hat{u}_k \, d\Gamma \; - \; \sum_{j=1}^{N_e} \int_{\Gamma_j} \Phi \, \hat{q}_k \, d\Gamma \right) . \tag{16}$$

The second approximation required by the BEM is functional. We approximate the variation of u and q within each element by writing them in terms of their values at some fixed points in the element (nodal points or nodes), using interpolation functions. The simplest possible approximation is a piece-wise constant one, which assumes that u and q are constant within each element and equal to their value at the midpoint. Using this approximation into Eq. (16), we obtain:

$$\begin{aligned} & c_i \, u_i \; + \; \sum_{j=1}^{N_e} u \int_{\Gamma_j} q^* \, d\Gamma \; - \; \sum_{j=1}^{N_e} q \int_{\Gamma_j} \Phi \, d\Gamma \; = \\ & \sum_{k=1}^{N_e \, + \, N_i} \mu_k \left(c_i \, \hat{u}_{ik} \; + \; \sum_{j=1}^{N_e} \hat{u}_k \int_{\Gamma_j} q^* \, d\Gamma \; - \; \sum_{j=1}^{N_e} \hat{q}_k \int_{\Gamma_j} \Phi \, d\Gamma \right) . \end{aligned} \tag{17}$$

Note that for the piece-wise constant elements boundary is smooth which means the free term $c_i \; = \; \frac{1}{2}$. Calling integrals:

$$G_{i\,j} \; = \; \int_{\Gamma_j} \Phi \, d\Gamma \, , \qquad H_{i\,j} \; = \; \int_{\Gamma_j} q^* \, d\Gamma \; + \; c_i \, \delta_{i\,j} \, , \tag{18}$$

where $\delta_{i\,j}$ is the KRONECKER delta:

$$\delta_{i\,j} = \begin{cases} 1, & \text{if } \; i \; = \; j, \\ 0, & \text{if } \; i \neq j. \end{cases} \tag{19}$$

The Eq. (17) can be rewritten as following:

$$\sum_{j=1}^{N_e} H_{ij} \, u_j \; - \; \sum_{j=1}^{N_e} G_{ij} \, q_j \; = \; \sum_{k=1}^{N_e \, + \, N_i} \mu_k \left(\sum_{j=1}^{N_e} H_{ij} \, \hat{u}_{jk} \; - \; \sum_{j=1}^{N_e} G_{ij} \, \hat{q}_{jk} \right) . \tag{20}$$

After application to all boundary nodes and computation of integrals Eq. (20) can be rewritten in the matrix form as:

$$\boldsymbol{H} \, \boldsymbol{u} \; - \; \boldsymbol{G} \, \boldsymbol{q} \; = \; \sum_{k=1}^{N_e \, + \, N_i} \mu_k \, (\boldsymbol{H} \, \hat{\boldsymbol{u}}_{\boldsymbol{k}} \; - \; \boldsymbol{G} \, \hat{\boldsymbol{q}}_{\boldsymbol{k}}) \, . \tag{21}$$

If each of the vectors $\hat{u}_k$ and $\hat{q}_k$ is considered to be one column of the matrices $\hat{\boldsymbol{U}}$ and $\hat{\boldsymbol{Q}}$ respectively, then Eq. (21) may be written without the summation:

$$\boldsymbol{H}\,\boldsymbol{u} \;-\; \boldsymbol{G}\,\boldsymbol{q} \;=\; \left(\boldsymbol{H}\,\hat{\boldsymbol{U}} \;-\; \boldsymbol{G}\,\hat{\boldsymbol{Q}}\right)\boldsymbol{\mu}\,. \tag{22}$$

The $\boldsymbol{\mu}$ vector in Eq. (22) is calculated as follows. By taking the value of b at $(\,N_e \,+\, N_i\,)$ different points, a set of equations like Eq. (8) is obtained. This may be expressed in matrix form as:

$$\boldsymbol{b} \;=\; \boldsymbol{F}\,\boldsymbol{\mu}\,, \tag{23}$$

where each column of $\boldsymbol{F}$ consists of a vector $\boldsymbol{f_k}$ containing the values of the function f_k at the $(\,N_e \,+\, N_i\,)$ collocation points. Now $\boldsymbol{F}$ can be inverted to obtain $\boldsymbol{\mu}$:

$$\boldsymbol{\mu} \;=\; \boldsymbol{F}^{-1}\,\boldsymbol{b} \;=\; \boldsymbol{F}^{-1}\,\dot{\boldsymbol{u}}\,, \tag{24}$$

where $\dot{\boldsymbol{u}} \;=\; \frac{\partial \boldsymbol{u}}{\partial t}$. Now Eq. (22) may be rewritten as:

$$\boldsymbol{H}\,\boldsymbol{u} \;-\; \boldsymbol{G}\,\boldsymbol{q} \;=\; \left(\boldsymbol{H}\,\hat{\boldsymbol{U}} \;-\; \boldsymbol{G}\,\hat{\boldsymbol{Q}}\right)\,\boldsymbol{F}^{-1}\,\dot{\boldsymbol{u}}\,. \tag{25}$$

The term multiplying $\dot{\boldsymbol{u}}$ can be seen as a "heat capacity" matrix and Eq. (25) can be rewritten in the form:

$$\boldsymbol{C}\,\dot{\boldsymbol{u}} \;+\; \boldsymbol{H}\,\boldsymbol{u} \;=\; \boldsymbol{G}\,\boldsymbol{q}\,, \tag{26}$$

where "heat capacity" matrix equal:

$$\boldsymbol{C} \;=\; -\left(\boldsymbol{H}\,\hat{\boldsymbol{U}} \;-\; \boldsymbol{G}\,\hat{\boldsymbol{Q}}\right)\,\boldsymbol{F}^{-1}\,. \tag{27}$$

System (26) is similar in form to the one obtained using the finite element method. Thus, any standard direct time-integration scheme can be used to find a solution to the above system. For higher accuracy, a three-level time integration scheme will be employed here in the form:

$$\dot{\boldsymbol{u}} \;=\; \frac{\left(3\,\boldsymbol{u}^{\,m\,+\,1} \;-\; 4\,\boldsymbol{u}^{\,m} \;+\; \boldsymbol{u}^{\,m\,-\,1}\right)}{2\,\Delta\,t}\,, \tag{28}$$

Substituting this approximation into Eq. (26) gives:

$$\left(\frac{3}{2\,\Delta t}\boldsymbol{C} \;+\; \boldsymbol{H}\right)\,\boldsymbol{u}^{m+1} \;-\; \boldsymbol{G}\,\boldsymbol{q}^{m+1} \;=\; \frac{4}{2\,\Delta t}\boldsymbol{C}\,\boldsymbol{u}^{m} \;-\; \frac{1}{2\,\Delta t}\boldsymbol{C}\,\boldsymbol{u}^{m-1}\,. \tag{29}$$

The right side of (29) is known at time $(m \;+\; 1)\,\Delta\,t$, since it involves values which have been specified as initial conditions or calculated previously. Upon introducing the boundary conditions at time $(m \;+\; 1)\,\Delta\,t$, which are of the convective type $q \;=\; -\,\mathrm{Bi}\,(\,u \;-\; u^{\infty}\,)$, $\boldsymbol{q}$ needs to be applied at all boundary nodes:

$$\boldsymbol{q} \;=\; \boldsymbol{D}\,\boldsymbol{u} \;+\; \boldsymbol{e}\,, \tag{30}$$

where the diagonal matrix $\boldsymbol{D}$ and the vector $\boldsymbol{e}$ contain the values of $(-\mathrm{Bi})$ and $(\mathrm{Bi}\,u^{\infty})$, respectively, at each boundary node. Substituting Eq. (30) into Eq. (29) yields the system of equations:

$$\left(\frac{3}{2\,\Delta t}\boldsymbol{C} \;+\; \boldsymbol{H} \;-\; \boldsymbol{G}\,\boldsymbol{D}\right)\,\boldsymbol{u}^{m+1} \;=\; \boldsymbol{G}\,\boldsymbol{e} \;+\; \frac{4}{2\,\Delta t}\boldsymbol{C}\,\boldsymbol{u}^{m} \;-\; \frac{1}{2\,\Delta t}\boldsymbol{C}\,\boldsymbol{u}^{m-1}\,, \tag{31}$$

which can be solved for the boundary values of temperature. Heat fluxes along the boundary may then be evaluated pointwise by using Robin boundary condition.

2.3.4 Numerical integration

Integration in Eq. (18) is carried out using composite SIMPSON's rule. Quadratic boundary elements are used to represent curved geometry. They provide increased accuracy because of their better representation of the variation of the functions along the boundary. The variation of coordinates $\boldsymbol{x}$ within each quadratic element is defined by their values at three global nodal points $\boldsymbol{x}^-$, $\boldsymbol{x}^o$, $\boldsymbol{x}^+$ using suitable interpolation functions, which are function of the homogeneous coordinate η:

$$\boldsymbol{x}\,(\,\eta\,) \;=\; N_1\,\boldsymbol{x}^- \;+\; N_2\,\boldsymbol{x}^o \;+\; N_3\,\boldsymbol{x}^+\,,$$

with

$$N_1 \;=\; \frac{1}{2}\,\eta\,(\,\eta \;-\; 1\,)\,, \qquad N_2 \;=\; (\,1 \;-\; \eta^2\,)\,, \qquad N_3 \;=\; \frac{1}{2}\,\eta\,(\,\eta \;+\; 1\,)\,,$$

η is the dimensionless coordinate varying $-1 \;\leq\; \eta \;\leq\; 1$. The difference with the numerical implementation of quadratic elements is that the Jacobian and normal vector are no longer constant within each element. In order to implement them, there is a need to transform from Cartesian to curvilinear coordinates [17]. The transformation from $d\Gamma$ to $d\eta$ is now given by:

$$d\Gamma \;=\; |\,J\,|\,d\eta,$$

with the Jacobian computed in the form:

$$|\,J\,| \;=\; \sqrt{J_x^2 \;+\; J_y^2} \;=\; \frac{d\Gamma}{d\eta}\,,$$

in which

$$J_x \;=\; \frac{dx}{d\eta}\,, \qquad J_y \;=\; \frac{dy}{d\eta}\,.$$

Hence one can write for Eq. (18):

$$G_{i\,j} \;=\; \int_{-1}^{1} \Phi\Big(\,\boldsymbol{x}\,(\,\eta_i\,)\,,\,\boldsymbol{x}\,(\,\eta\,)\,\Big)\,|\,J\,|\,d\eta\,.$$

Similarly, other integrals can be computed. The components of the unit normal vectors at any point are given by:

$$n_x \;=\; \frac{J_y}{|\,J\,|}\,, \qquad n_y \;=\; -\,\frac{J_x}{|\,J\,|}\,.$$

3 DESIGN OPTIMIZATION PROBLEM

The objective of this work is to optimize energy efficiency of a building wall by finding the optimal shape of the left boundary Γ_1 which is in contact with outside environment. In general, heat transfer design objectives can be classified into two categories: *(i)* heat transfer augmentation problems and *(ii)* thermal insulation problems. Thus, the optimization problem aims at finding parameters of the left boundary that minimizes the following cost function:

$$\boldsymbol{p}^\circ \;=\; \arg\min_{\boldsymbol{p}\,\in\,\Omega_p} \mathcal{J}\,(\,\boldsymbol{p}\,)\,, \tag{32}$$

where the objective function $\mathcal{J}\,\big[\,\mathrm{W}\,.\,\mathrm{m}^{-2}\,\big]$ is the averaged inward heat flux on the right boundary, corresponding to the inside of the building:

$$\mathcal{J}\,(\,\boldsymbol{p}\,) \;=\; \sigma\frac{1}{H\,t_\infty}\int_0^{t_\infty}\!\!\int_0^{H} -k\,\boldsymbol{\nabla}\,T\;(\,\gamma\,(\,\boldsymbol{p}\,,\,y)\,)\;\vec{\boldsymbol{n}}\,dy\,dt\,, \tag{33}$$

where σ is the parameter which takes values -1 and 1. In other words the first case requires the highest thermal conductance for the heat transfer augmentation. Consequently, in the second case the thermal conductance is the lowest for the thermal insulation problems. Note that the objective function needs to be optimized under several constraints. First, the physical area of the wall $S(\boldsymbol{p})$ should not exceed the reference case area S_∞. The reference case is defined as the flat standard wall ($\gamma = 0$ in Eq. (1)). Thus, the cost function Eq. (33) needs to be optimized under the following constraint:

$$S(\boldsymbol{p}) \leq S_\infty,$$

which, given the representation in Figure 1, leads to:

$$\int_{\Gamma_3} L\, d\Gamma - \int_{\Gamma_1} \gamma(\boldsymbol{p}, y)\, d\Gamma \leq \int_{\Gamma_3} L\, d\Gamma,$$

which can be rewritten as

$$\int_{\Gamma_1} \gamma(\boldsymbol{p}, y)\, d\Gamma \geq 0. \tag{34}$$

The second constraint that must be satisfied by the parametrized mapping is that the maximum width of the wall cannot be higher than L. In other words, the left and right boundaries cannot overlap:

$$\gamma(\boldsymbol{p}, y) \leq L - \delta, \tag{35}$$

where δ is a given spatial tolerance.

The extremums of cost function Eq. (33) are found with trust region method using exhaustive search results as an initial values for parameters[20]. Trust-region method first defines a region around the current best solution, in which a certain model (usually a quadratic model) can, to some extent, approximate the original objective function. Trust-region method then take a step forward according to the model depicts within the region. Unlike the line search methods, such method usually determines the step size before the improving direction.

4 VERIFICATION OF THE NUMERICAL MODEL

Exact solution u_e for Eq. (2) is used as a reference for verification of numerical solutions:

$$u_e(\boldsymbol{x}) = \frac{x^4 y^4 t}{12} + 2x^2 t^2 - 2y^2 t^2. \tag{36}$$

The boundary conditions will be in the following sections. The verification will be carried for rectangular domain with the $L = 0.25$ and $H = 0.5$. Thus, it corresponds to a flat facade with mapping function $\gamma(\boldsymbol{P}, y) = 0$. Since the objective of this work lies on computation of fluxes on boundaries, the following boundary conditions are considered for the problem Eq. 2:

$$u = u_e(\boldsymbol{x}), \qquad \forall x \in \Gamma_1 \cup \Gamma_2 \cup \Gamma_3 \cup \Gamma_4,$$

To compute analytical solution $q_e(\boldsymbol{x})$ for fluxes on boundaries, one has to take normal derivatives of $\hat{u}$. The analytical solution is compared with the BEM as well as the finite-difference method (FDM). The latter is implemented using the alternating-direction implicit (ADI) method. For the numerical solution output q, the error ε_2 is computed according to:

$$\varepsilon_2 \circ q = ||q - q_e||_2.$$

The fluxes q are computed for all boundary points. Different values of the time step Δt are chosen.

Figure 3(a) presents the error according the time step of method for BEM and FDM. It illustrates unconditional stability of the BEM and highlights that time step doesn't have impact to the BEM accuracy comparing to FDM. It highlights that BEM results has a significant lower error compared to FDM results for bigger time step values. Figure 3(b) shows the error according the spatial step of each method. The BEM approach has an error behaviour around $\mathcal{O}(\Delta h)$ in contrast with FDM approach, which has second order behaviour. In addition to that, the BEM approach shows better accuracy for bigger values of spacial step. Thus, overall the BEM method is suitable for problems which demand high memory storage and time computation.

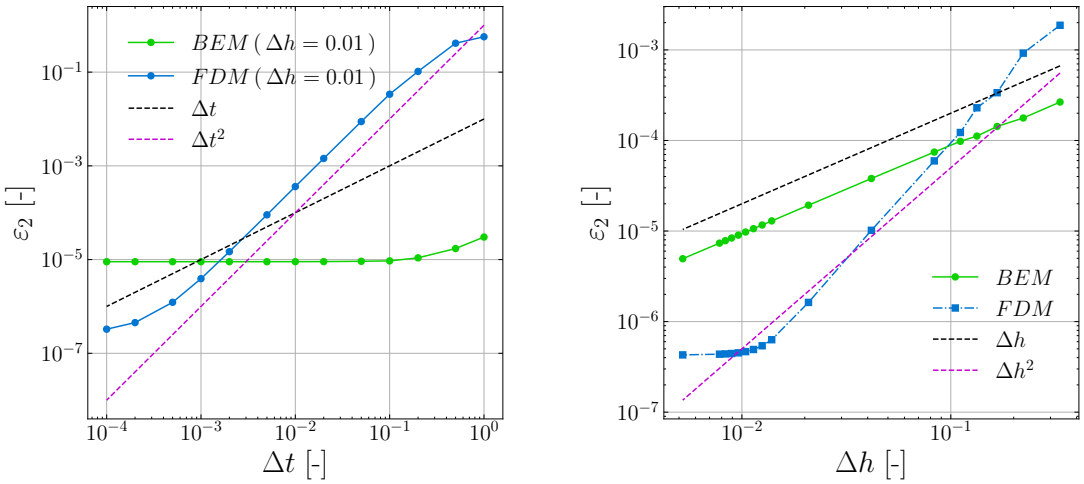

(a) (b)

Figure 3. *Influence of time step* Δt *on* ε_2 *error for dimensionless* q *at* $t = 1$ *for spacial step value* $\Delta h = 0.01$ (a) *and influence of spacial step* Δh *on* ε_2 *error* (b).

5 CASE STUDY

5.1 Presentation

Since the BEM numerical method have been verified, a real case study is now investigated for optimization of the thermal design of a building facade. Case study considers a house wall for two different days with opposite climate conditions (winter and summer) from 9 h to 18 h in Nice city, France. The initial condition is assumed to be interpolation of measured temperature. Thus, first order polynomials of $x \in [0, L]$ are fitted the temperature distribution in the wall.

$$T^0(\boldsymbol{x}) = \frac{(T_R^0 - T_L^0) \cdot x}{L} + T_L^0, \; x \in [0,\, L]. \tag{37}$$

Time step $\Delta t = 6\,\mathsf{min}$. The wall is composed of bricks with thermal diffusivity $\frac{k}{\rho\, c_p} = 1\,\mathsf{m}^2\,.\,\mathsf{s}^{-1}$. The height and width of the wall are $H = 3\,\mathsf{m}$ and $L = 0.3\,\mathsf{m}$. T_R, T_L, v_∞ are taken from standard climatic data [16]. The absorptivity of the right boundary is set to $a = 0.5$. The incident radiation flux are computed using analytical projections of the solar angle, considering shadow induced by front building and by the own shape of the boundary Γ_1. For the boundary Γ_1, other coefficients are taken as $h_0 = 5.82\ \mathsf{W}\,.\,\mathsf{m}^{-2}\,.\,\mathsf{K}^{-1}$, $h_1 = 3.96\ \mathsf{W}\,.\,\mathsf{m}^{-2}\,.\,\mathsf{K}^{-1}$, $\lambda = 0.32$, $v_0 = 1\ \mathsf{m}\,.\,\mathsf{s}^{-1}$, $y_0 = 65.33\ \mathsf{m}$. Regarding the urban environment, two values of ratio between front building distance D_x m and height D_y m are considered as presented in Table 1. This choice ensure to have a sunlit on the facade and ensure a possible shape optimization of the facade [16]. The shape optimization is carried out for two dates (December 21^{st} and June 21^{st}).

December 21^{st} is chosen for heat transfer augmentation problem, since it aims to increase the rate of heat transfer in winter period. Inversely, June 21^{st} is considered for thermal insulation, since it aims to reduce heat transfer in summer period.

5.2 Results

The number of boundary elements is set to $N_e = 256$. The spatial tolerance is set to $\delta = 0.25\,L$. For the mapping function γ Eq. (1), a third order polynomial is considered:

$$\gamma(\boldsymbol{p}, y) = p_0\, y \left(\frac{y}{H} - p_1\right)\left(\frac{y}{H} - 1\right) - \frac{H\, p_0}{12}(2\, p_1 - 1).$$

With such equation, parameter p_0 states the convexity of the shape and p_1 the roots of the equation. As described in Section 3, area and boundary constraints (Eq. (34) and Eq. (35)) have to be satisfied. Application of those constraints for the given mapping function is demonstrated in [16]. As a result, we have:

$$p_1 \in [0, 1], \qquad \hat{p}_0^-(p_1) \leq p_0 \leq \hat{p}_0^+(p_1),$$

where $\hat{p}^-$ and $\hat{p}^+$ are constraint functions which are illustrated in Figure 4(a). Note that it is a connected space.

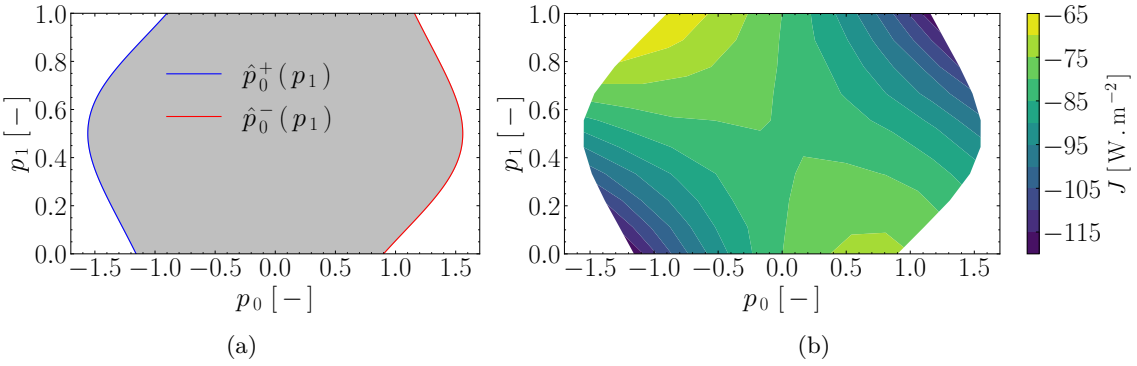

Figure 4. *Domain of* $\boldsymbol{p}$ *variation* (a) *and the distribution of the objective function value in the domain resulting from the exhaustive search* (b).

First analysis focuses on the heat transfer augmentation problem on December 21^{st}. After preliminary analysis using exhaustive search method the objective function distribution is shown in Fig. 4(b). A grid of 10×10 parameters equally spaced between the bounds is defined for exhaustive search method. The cost function has monotonous behaviour. Thus, to increase convergence rate one can use extremum values from this exhaustive search results as a initial parameters for the optimization method. The flat wall reference $\boldsymbol{p}_{ref}$ and optimized wall $\boldsymbol{p}^\circ$ parameters are given in Table 1. In addition, the reference flat wall and the optimized shapes with corresponding SWR and heat flux at midday on inside and outside surfaces of the wall are illustrated in Fig. 5. In case of the heat transfer augmentation the heat transfer is increased by 52%. Figure 5(b) reveals that it is achieved due to concavity on the top of the wall and convexity on the bottom, which lead to higher magnitude of short wave radiation at Γ_1 (Fig. 5(a)) and as a consequence of the heat flux on the inside surface Γ_3 (Fig. 5(c)).

Second analysis deals with thermal insulation problem on June 21^{st}. Results are presented in Table 1, which shows optimization for energy efficiency from reference case. Figure 6(b) illustrates that in case of thermal insulation problem optimized shape shows opposite pattern then in the heat transfer augmentation case. The heat transfer is decreased by 16%. Such behaviour appeared due to convexity on the top of the wall and concavity on the bottom. It

Table 1. *Optimization results.*

	Cost function value			Optimized shape parameter		Neighbour building
Day	$\mathcal{J}(\boldsymbol{p}_{ref})$	$\mathcal{J}(\boldsymbol{p}^\circ)$	$\mathcal{J}(\boldsymbol{p}^\circ)/\mathcal{J}(\boldsymbol{p}_{ref})$	p_0°	p_1°	$D_x\,/\,D_y$
heat transfer augmentation problems						
December 21st	−6.368	−3.086	0.484	−0.9	0.999	0.8
thermal insulation problems						
June 21st	19.905	16.704	0.839	0.437	0.999	0.3

imply a decrease of the incident short wave radiation at Γ_1 (Fig. 6(a)) and of the heat flux at Γ_3 (Fig. 6(c)). It is due to the change of the angle between the direct beam and the normal facade surface that affects the direct flux component q^{dr}. Note that results are depicted for midday values only.

To sum up all above, the influence of the shape of the wall and shadow distribution along surface is significant for optimization of energy efficiency in the buildings. Figure 7(a) shows distribution of the shadow on wall's surface during the day H_s and according to Fig. 7(b), considerable impact can be seen when wall partially under the shadow.

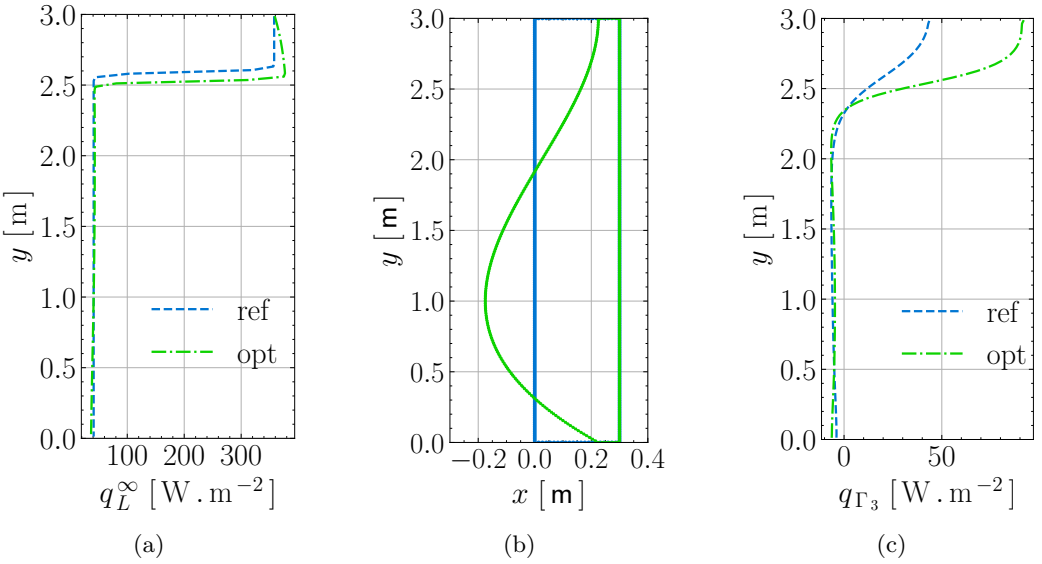

Figure 5. *Comparison of the reference and optimized wall shapes* (b) *with corresponding SWR distributions* (a) *and flux q on* Γ_3 (c) *on December 21st for the heat transfer augmentation problem. The green line corresponds to the optimized data.*

Another important point regarding the optimized wall shapes is that in both cases of heat transfer augmentation and thermal insulation the total area of the wall is the same as in the reference flat case. Thus, from engineering point of view there is no need for additional materials compared to the reference flat wall.

6 CONCLUSION

This article explores the optimization of wall shapes to enhance energy efficiency by considering incident radiation, which is influenced by the wall's surface shape. Initially, the Boundary Element Method is employed to model the complex geometry of the non-flat wall and predict transient heat transfer phenomena in the two-dimensional structure. The validity of the BEM

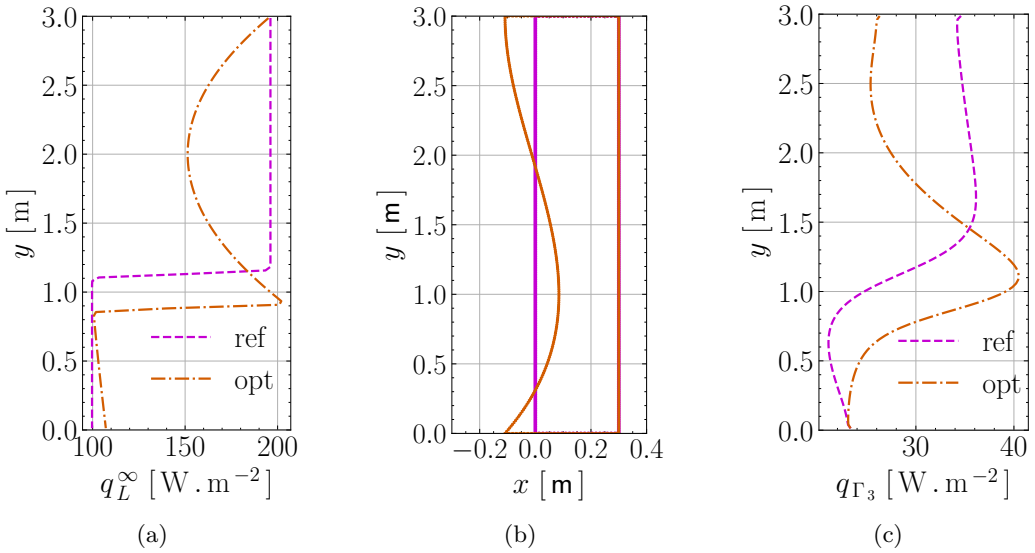

Figure 6. *Comparison of the reference and optimized wall shapes* (b) *with corresponding SWR distributions* (a) *and flux* q *on* Γ_3 (c) *on June 21st for the thermal insulation problem. The orange line corresponds to the optimized data.*

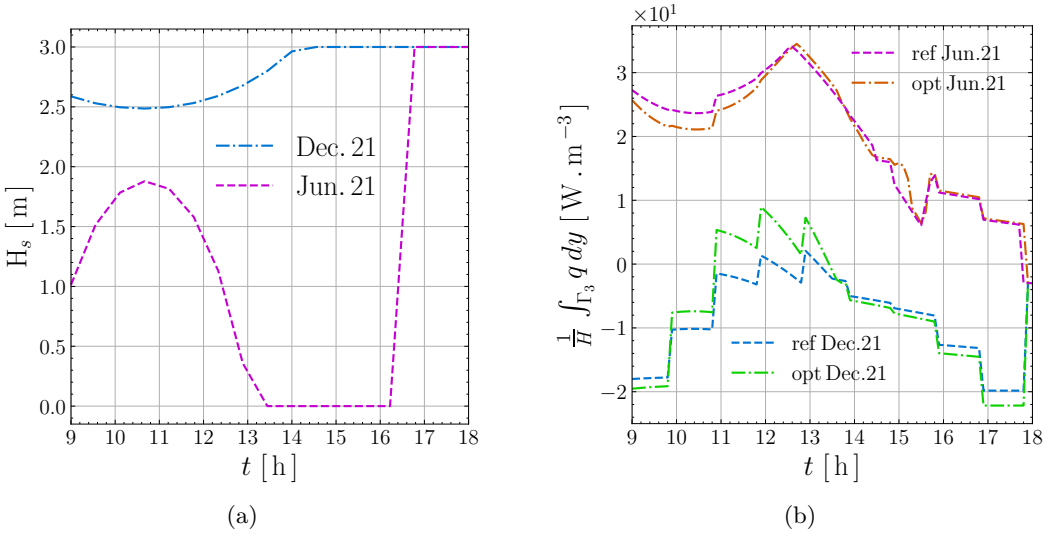

Figure 7. *Variation of the shadow height induced by the front building on the reference wall* (a) *and of the average flux* q *on* Γ_3 (b) *on December 21st and June 21st respectively.*

model is confirmed through comparison with an analytical solution and the finite difference method. The numerical findings emphasize that the Boundary Element approach is both faster and with increase stability compared to conventional finite-difference methods.

Subsequently, a practical case study is undertaken to enhance the energy efficiency of a building wall, focusing on a house wall located in the south-east of France where radiation levels are substantial. Two heat transfer design objectives are considered: (i) increasing heat transfer and (ii) improving thermal insulation. The results indicate that these objectives can be achieved without the addition of materials. Specifically, the energy efficiency can be enhanced by two times in winter and 16% in summer, respectively.

Future research should prioritize simulation for longer time period with inclusion of the night time. Regarding the shape optimization of building enclosures, there is a need to explore various

approaches for parameterizing the wall domain.

7 ACKNOWLEDGEMENTS

The authors acknowledge the French National Research Agency (ANR) as part of the "JCJC CE-22 AAPG 2023" program (project TOPS) for the financial support.

8 REFERENCES

References

[1] International Energy Agency. Building global energy consumption, 2022. 1

[2] Adriana Ciardiello, Federica Rosso, Jacopo Dell'Olmo, Virgilio Ciancio, Marco Ferrero, and Ferdinando Salata. Multi-objective approach to the optimization of shape and envelope in building energy design. *Applied Energy*, 280:115984, 2020. 1

[3] Julien Berger and Nathan Mendes. An innovative method for the design of high energy performance building envelopes. *Applied Energy*, 190:266 – 277, 2017. 1

[4] Nicolas Lauzet, Auline Rodler, Marjorie Musy, Marie-Hélène Azam, Sihem Guernouti, Dasaraden Mauree, and Thibaut Colinart. How building energy models take the local climate into account in an urban context – a review. *Renewable and Sustainable Energy Reviews*, 116:109390, 2019. 1

[5] Mohammad Jafari and Alice Alipour. Methodologies to mitigate wind-induced vibration of tall buildings: A state-of-the-art review. *Journal of Building Engineering*, 33:101582, 2021. 1

[6] Christina Diakaki, Evangelos Grigoroudis, and Dionyssia Kolokotsa. Towards a multi-objective optimization approach for improving energy efficiency in buildings. *Energy and Buildings*, 40(9):1747–1754, 2008. 1

[7] Yunfeng Luo, Wenjiong Chen, Shutian Liu, Quhao Li, and Yaohui Ma. A discrete-continuous parameterization (dcp) for concurrent optimization of structural topologies and continuous material orientations. *Composite Structures*, 236:111900, 03 2020. 1

[8] José Meissner, Marc Abadie, Luís Moura, Kátia Mendonça, and Nathan Mendes. Performance curves of room air conditioners for building energy simulation tools. *Applied Energy*, 129:243 – 252, 2014. 2

[9] Abdollah Baghaei Daemei and Seyed Eghbali. Study on aerodynamic shape optimization of tall buildings using architectural modifications in order to reduce wake region. *Wind and Structures An International Journal*, 29:139–147, 08 2019. 2

[10] Mayssa Dabaghi Aram Yeretzian, Hmayag Partamian and Rabih Jabr. Integrating building shape optimization into the architectural design process. *Architectural Science Review*, 63(1):63–73, 2020. 2

[11] Yukinori Kametani, Yutaka FUKUDA, Takayuki OSAWA, and Yosuke HASEGAWA. A new framework for design and validation of complex heat transfer surfaces based on adjoint optimization and rapid prototyping technologies. *Journal of Thermal Science and Technology*, 15(2):JTST0016–JTST0016, 2020. 2

[12] Louis S.H. Lee and C.Y. Jim. Energy benefits of green-wall shading based on novel-accurate apportionment of short-wave radiation components. *Applied Energy*, 238:1506–1518, 2019. 3

[13] W. H. McAdams. *Heat Transmission*. 1985. 3

[14] Efim G. Evseev and Avraham I. Kudish. The assessment of different models to predict the global solar radiation on a surface tilted to the south. *Solar Energy*, 83(3):377–388, 2009. 3

[15] A. H. Nayfeh and Vimal Singh. Perturbation methods. *IEEE Transactions on Systems, Man, and Cybernetics*, 8(5):417–418, 1978. 3

[16] Sultan Alpar, Julien Berger, Walter Mazuroski, and Rafik Belarbi. Shape optimisation of the energy efficiency of building retrofitted facade. *Solar Energy*, 2024. 3, 10, 11

[17] Luiz Wrobel. *The Boundary Element Method: Application in Thermo-Fluids and Acoustics*. 01 2002. 4, 8

[18] D.P.N. Kontoni, P.W. Partridge, and C.A. Brebbia. The dual reciprocity boundary element method for the eigenvalue analysis of helmholtz problems. *Advances in Engineering Software and Workstations*, 13(1):2–16, 1991. 4

[19] L. Marin. Numerical boundary identification for helmholtz-type equations. *Computational Mechanics*, 39:25–40, 12 2006. 6

[20] Zongyi Xing, Zhenyu Zhang, Jian Guo, Yong Qin, and Limin Jia. Rail train operation energy-saving optimization based on improved brute-force search. *Applied Energy*, 330:120345, 2023. 9